Two step phase transition in SnSe and the origins of its high powerfactor from first principles : Supplementary informations

Antoine Dewandre,[1,2] Olle Hellman,[3,4] Sandip Bhattacharya,[5] Aldo H. Romero,[6] Georg K. H. Madsen,[5] and Matthieu J. Verstraete[1,2]

[1] *Department of Physics, Université de Liège, allée du 6 août, 17, B-4000 Liège, Belgium.*
[2] *European Theoretical Spectroscopy Facility www.etsf.eu*
[3] *Division of Engineering and Applied Science, California Institute of Technology, Pasadena, California 91125.*
[4] *Department of Physics, Chemistry and Biology (IFM), Linköping University, SE-581 83, Linköping, Sweden*
[5] *ICAMS, Ruhr-Universität Bochum, 44780 Bochum, Germany*
[6] *Department of Physics, West Virginia University, 207 White Hall, 26506, WV, USA.*

(Dated: August 25, 2016)

STRUCTURES

The calculations of the relaxed structures are carried out using density functional theory (DFT) formalism, as implemented in the ABINIT code[1, 2]. Norm-conserving Troullier-Martins type pseudo-potentials generated with fhi98PP code are used to describe interactions between ions and electronic density. The exchange-correlation energy is given by the generalized gradient approximation (GGA) of Perdew, Burke and Ernzerhof. The wave functions are represented in a plane-wave basis set with a cutoff energy of 30 Ha. Some calculations are confirmed at a cutoff of 40 Ha. The reciprocal space of the low-temperature phase (Pnma) is sampled with a $4 \times 4 \times 4$ Monkhorst-Pack-type grid [3], whereas for the high-temperature phase (Cmcm) and the cubic phase, an $8 \times 8 \times 8$ unshifted grid was used. The total energy of both phases is converged to within 3 meV. Atomic positions and lattice parameters are relaxed using a Broyden algorithm where a maximal absolute force over atoms of 10^{-6} Ha/Bohr is set as a stopping criterion for the relaxation.

The Pnma phase is made up of two-dimensional layers stacked along the c axis. The layers have a weak interaction which controls the global structural properties. Anions and cations form layers in a zig-zag pattern of chains. Each atom has four neighbours with covalent bonding.

In the past, many groups studied the low T Pnma phase, few studied the high T Cmcm phase. To our best knowledge, only Ref. [4] have investigated the high T phase theoretically and used experimental structure from Ref. [5]. Overall, we have a good agreement for the Pnma with the structures of other groups. For the Cmcm phase, we have a good agreement with experimental data : while the a and b axis are slightly underestimated, the c axis is overestimated. The differences result from three sources: common overestimation due to the GGA, the pseudopotential approximation; the lack of thermal expansion comparing to high temperature lattice constants; and the lack of Van der Waals corrections.

Calculations of the Cubic phase of SnSe are also presented here. This structure is not a natural phase of SnSe because the melting of SnSe appears before the phase transition from Cmcm to Cubic phase. However, this phase can be induced by pressure and has interesting superconducting properties [6].

Table I summarizes the different cell parameters used here and found in the literature.

Pnma

	Pseudo-potentials	Cell parameters		
Zhao et al. [5]		4.22	4.40	11.58
Sassi et al. [7]		4.153	4.433	11.497
Chattopadhyay et al. [8] at 295 K		4.153	4.445	11.501
Chattopadhyay et al. [8] at 790 K		4.282	4.334	11.580
Relaxed structure	GGA PBE FHI	4.2095	4.4968	11.7201
Carrete et al. [9]	LDA PAW	4.20	4.55	11.72
Guo et al. [10]	LDA PAW PW	4.12	4.29	11.31
Guan et al. [11]	GGA PBE SOC	4.190	4.46	11.570

Cmcm

	Pseudo-potentials	Cell parameters		
Zhao et al. [5]		4.31	4.31	11.70
Chattopadhyay et al. [8] at 825 K		4.318	4.310	11.705
Relaxed structure	GGA PBE FHI	4.2838	4.2816	11.9025
Modified Cmcm	GGA PBE FHI	4.2816	4.2838	11.9025

Cubic

	Pseudo-potentials	Cell parameters		
Relaxed structure	GGA PBE FHI	6.0468	6.0468	6.0468

TABLE I. Summary of the experimental and theoretical structures used for our calculations and found in the literature. The relaxed structures are used to calculate harmonic and anharmonic phonons. Structures from Ref. 8 are used to calculate electronic band structures, defect formation energies and Seebeck coefficients.

ELECTRONIC BAND STRUCTURE

Electronic band structures were calculated with Wien2k code [12] using the exchange correlation functional of Engel-Vosko [13] on a finer $35 \times 33 \times 12$ k-point grid for the Pnma phase and $25 \times 25 \times 23$ k-point grid for the Cmcm phase. Figure 1 shows electronic band structures for Pnma phase at 298 and 790 K as well as that of the Cmcm phase at 825K. For the Pnma structures the bandgap is 0.96 eV at 298 K which decreases to 0.90 eV at 790K. For the Cmcm structure the bandgap is 0.77 eV.

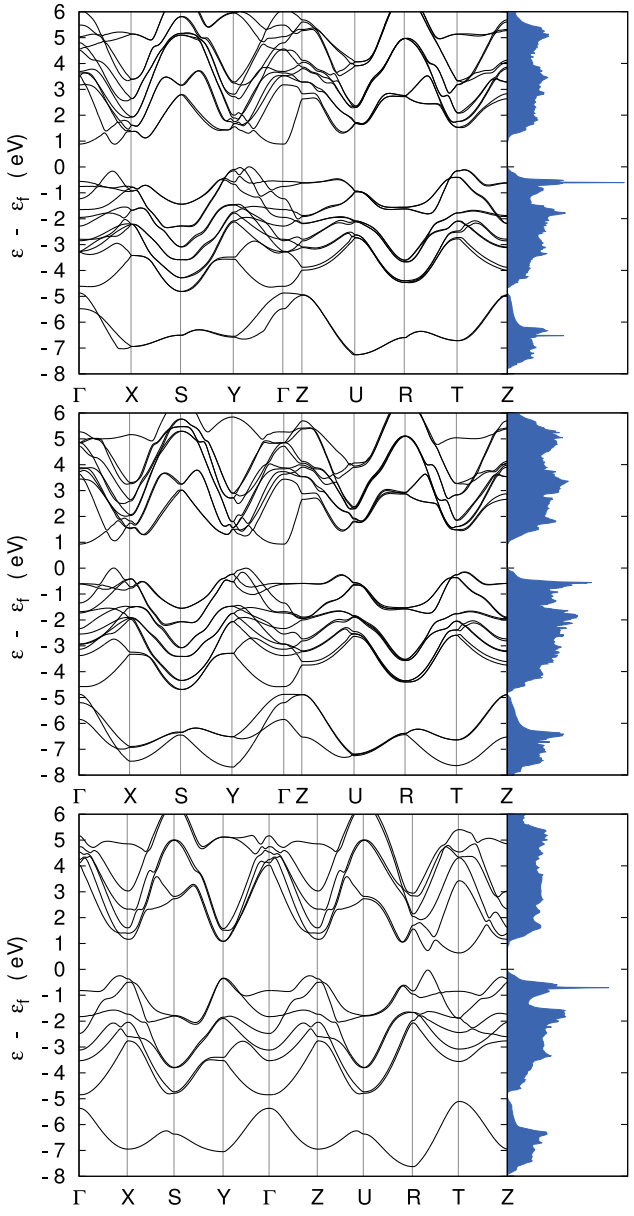

FIG. 1. Electronic band structures Pnma structure with experimental volume taken at 298 K and 790 K, and Cmcm structure with experimental volume at 825K.

HARMONIC PHONON BAND STRUCTURES

Phonon band structures along high symmetry lines have been obtained by standard methods based on response function calculations and DFPT[14] with the ABINIT code. Respectively twenty-nine (Pnma), twenty-one (Cmcm) and eight (Cubic) irreducible q-points were taken from an unshifted $4 \times 4 \times 4$ grid of k-points and used for the interpolation of interatomic force constants (IFC). Pnma phonon band structure (Fig. 2) shows a gap of around 4 cm^{-1} and there are several crossing points along the $\Gamma - X$ and $\Gamma - Y$ directions that we should expect to be quite temperature dependent as is the case in PbTe [15]. The strongest differences between experimental and theoretical phonon frequencies at Γ lies below 10 %, except for LO modes which are strongly underestimated. Cmcm phonon band structure (Fig. 3) presents an unstable phonon mode at Γ. Cubic phonon band structure is presented in Fig. 4. No unstable phonon modes and some band crossing can be observed. The first characteristic demonstrate the metastablility of the structure and the second gives hint of good thermal properties as in PbTe [15].

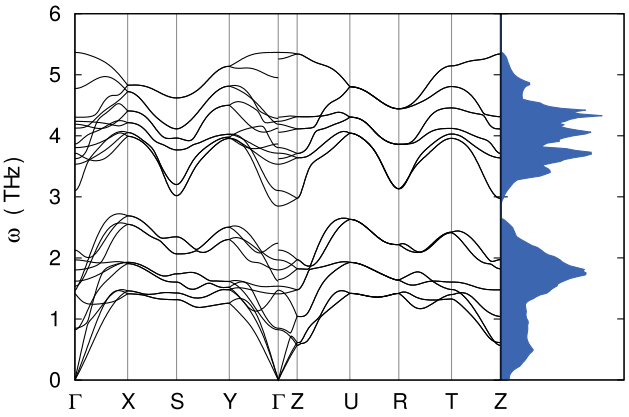

FIG. 2. Pnma phonon band structure.

ANHARMONIC HIGH-TEMPERATURE PHONONS

To accurately describe the high temperature anharmonicity of SnSe we used *ab initio* molecular dynamics in combination with the temperature dependent effective potential technique (TDEP)[16, 17] to extract effective interatomic force constants at finite temperature. The *ab initio* molecular dynamics was carried out with the the projector augmented wave (PAW)[18] method as implemented in VASP.[19–22] Exchange-correlation was treated with the Perdew-Burke-Ernzerhof functional form.[23] The simulation cell was constructed from a $4 \times 4 \times 4$ repetition of the unit cell (256 atoms). We used a

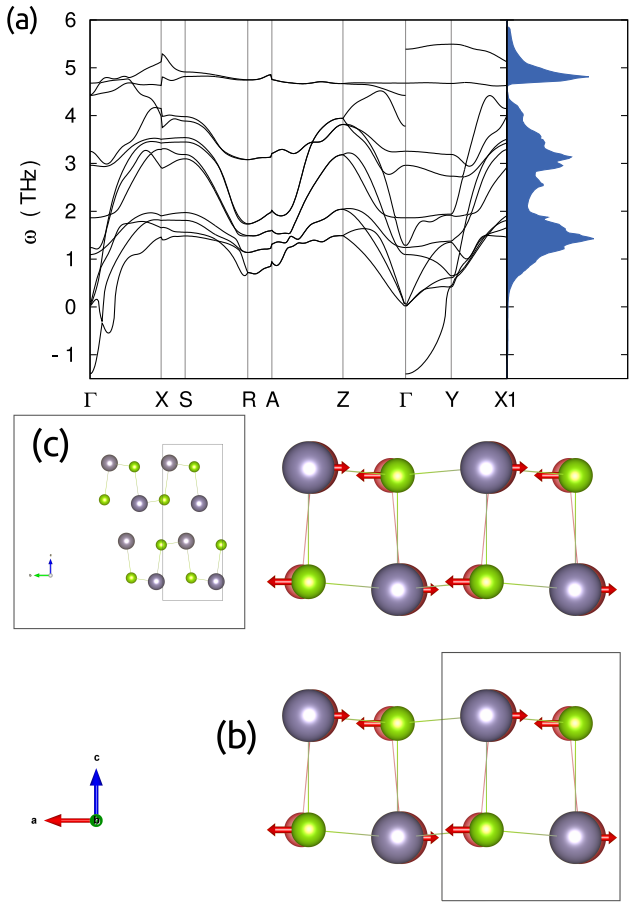

FIG. 3. (a) Cmcm phonon band structure. An unstable phonon mode at Γ distorts the Cmcm structure as shown in (b). This distorted structure does not correspond to the Pnma structure (c). Eigenvectors (red arrows) show that distortions appear only along the a axis and alternate the bond lengths between Sn and Se along that axis. In this distorted structure appears one of the main characteristics of the Pnma, i.e. the dimerization along one of the inter-plane axis. However, the dimerized axis in Pnma is the b axis. Thus, the unstable phonons are not responsible for the full transition from Cmcm to Pnma.

set of seven volumes around equilibrium and ran molecular dynamics at 800K using the Γ-point for Brillouin zone integration and an energy cutoff of 400 eV for about 10000 time steps starting from 5 different random seeds to ensure good phase space coverage. The temperature was controlled with a Nose-Hoover thermostat[24, 25]. A 2 femtosecond time step was used in the molecular dynamics calculations. Out of the 10000 timesteps 30 were randomly chosen, recalculated using a $2 \times 2 \times 2$ k-point grid, and interatomic force constants were extracted. The equilibration time of each MD simulation has been greatly reduced by starting from uncorrelated samples corresponding to a canonical ensemble. These initial guesses were already thermalised using the method described in Ref. [26].

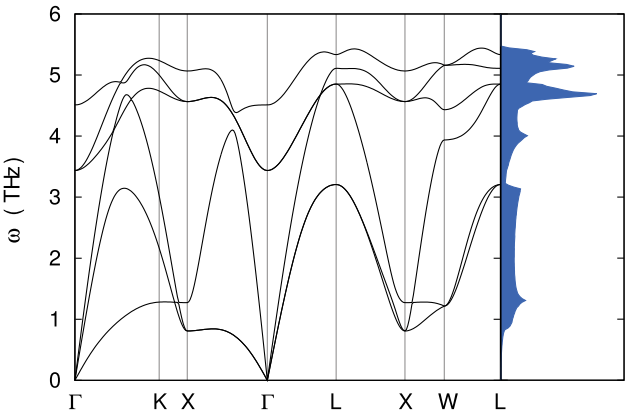

FIG. 4. Cubic phonon band structure. The absence of unstable phonon mode proves the metastable character of the structure at 0 K.

METADYNAMICS

The crystal structural transition involves energies that can be difficult to describe by normal Ab initio molecular dynamics due to limitations in simulation time and thermodynamic sampling. In order to overcome this, a method was introduced in 2003 by Martoňák, Laio and Parrinello [27, 28] known as metadynamics for crystals. In this methodology, the Gibbs potential G is defined as a function of the collective variable $\mathbf{h}$, which is the matrix defined by lattice vectors as $\mathbf{h} = \vec{a}, \vec{b}, \vec{c}$. The matrix $\mathbf{h}$ is evolved by a steepest descent algorithm, driving the system to a minimum of G. The key in metadynamics is the introduction of a history dependent repulsive potential in the Lagrangian, given by a series of Gaussians that are added at each time step. The presence of this potential drives the system out of its instantaneous minimum, and allows the structure to evolve to other configurations and explore the potential energy surface. The calculations reported in this work follow exactly the implementation discussed in Refs. [27–29].

The computational details for the metadynamics are as follows. The ab initio molecular dynamics was obtained using the VASP code.[19–22] Exchange-correlation was treated with the Perdew-Burke-Ernzerhof functional form. Similar calculations were also performed by considering the PBEsol as the exchange correlation functional [33], with similar results. The initial state was built from an optimized Pnma cell of 8 atoms, and several calculations were performed with supercells of 3x3x3 and 3x3x2, for a total of 216 atoms and 144 atoms respectively. Short molecular dynamics of 300 fs with a Nosé thermostat [30–32] are used to estimate the average stress tensor at each metadynamic step. The MD is performed with only Γ point sampling of the Brillouin Zone - we have checked that the energy ordering of the Pnma, Cmcm, and rocksalt phases is correct even with

the reduced sampling. For the Gaussian history term, our reported results are obtained with a gaussian width of σ of 10 (kbar Å^3)$^{(1/2)}$ and a Gaussian height of 100 kbar Å^3 (taken to be σ^2 to obtain a normalized Gaussian). We have also tested with values for σ of 20 (kbar Å^3)$^{(1/2)}$ and 40 (kbar Å^3)$^{(1/2)}$.

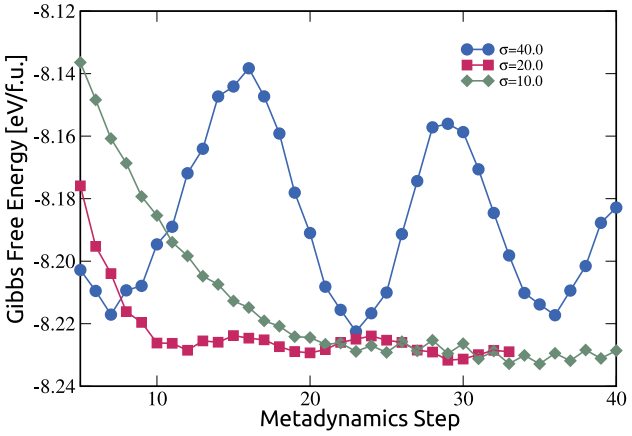

FIG. 5. Gibbs free energy obtained from metadynamics for T = 300K. Different gaussian widths were considered, starting from $\sigma = 40, 20$ and 10. The last two cases see the same potential energy surface, while for $\sigma = 40$, the metadynamics gets rather quickly to a minima and large oscillations are observed, while each of the minima corresponds to a cubic like structure.

Figure 5 shows the evolution of the Gibbs free energy per formula unit as a function of the metadynamics step for $T = 300K$ and with the PBE functional. For $\sigma = 40$, the metadynamics oscillates quite quickly and strongly, while the changes for $\sigma = 10$ and 20 are smaller and do not show important differences. A first new minimum of the PES is reached within 10-20 iterations. During this period, there is a relative shift between the SnSe bilayers towards a rocksalt-like stacking. After this shifting settles, the structure oscillates between different minima in Gibbs Free Energy, with $b/a > 1$ and $b/a < 1$.

To characterize the proximity of the system to Pnma, Rocksalt, and Cmcm structures, Figure 6 shows histograms of the average Sn-Se distances, binned over the last 150 fs in the MD runs of different metadynamics steps. At step 1 the Sn-Se distances correspond retains some of the Pnma (energy miminization of the final structure of step 1 identifies space group 62). Temperature seems to be a stronger driving force than the Gaussians, in the relative shifting between the SnSe layers, as it is already present in metadynamics step 1. In very few iterations, the Free energy is reduced to the closest minimum that corresponds to a b/a ratio close to 1.0. This indicates that the transition from the Pnma phase almost barrierless. After iteration 20, the structure presents one broad peak with an Sn-Se average bond length in plane of 3.02 Å. This is close to distances present in the rockstalt case (3.028 Å) and Cmcm (3.054 Å), but the shorter bond in

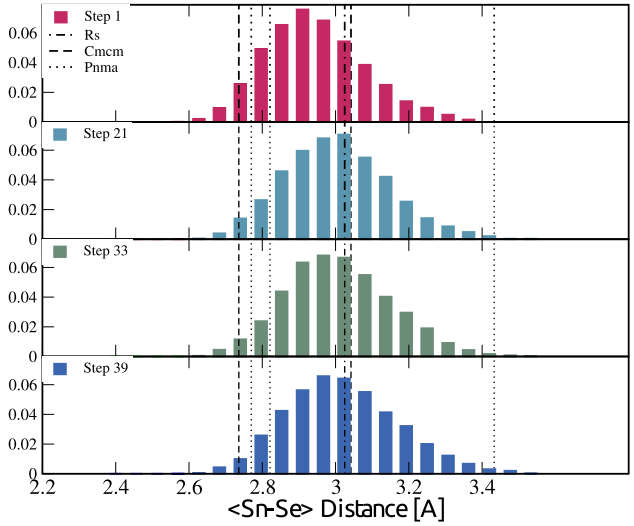

FIG. 6. Average atomic Sn-Se distance at different metadynamics steps for T = 300K and $\sigma = 10$. Dotted line corresponds to the relaxed Pnma phase, dotted-dashed is the relaxed rockstalt phase and the dashed line is the relaxed Cmcm phase, all at 0K.

Cmcm is missing. The peak shifts gradually to larger values up to iteration 20 and then it oscillates around 2.92 Å. The lower right panel of Fig 6 (main paper) shows that the scalar product of generalized forces is never positive after the layer slip occurs: the system never falls into another separate well. Neither does it attain the value of -1, which would indicate the metadynamics is climbing straight out of a well in the PES. The image is that of continuous rotation in a large and flat well in the PES. Based on the lattice parameter ratio and the behavior of the histogram we conclude that the structure moves from the Pnma phase to rocksalt with very little initial barrier to the bilayer "slip". The b/a ratio is close to one, but the system retains some local memory of the anisotropy of Pnma and Cmcm in the asymmetry of the bond length peak. The metadynamics clearly shows the path from Pnma towards rocksalt, and the results do not show any presence of a Cmcm phase, even at 700K.

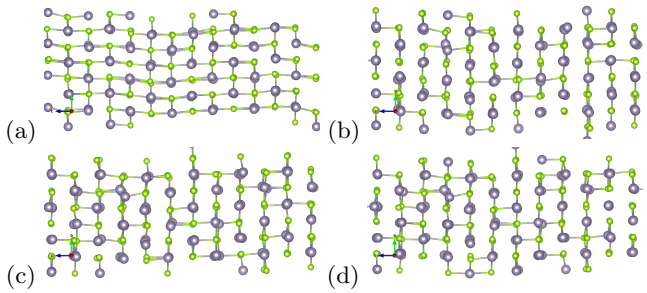

FIG. 7. Metadynamics snapshots after the molecular dynamics run at each particular metadynamics states at T = 300K and $\sigma = 10$. (a) Step 1 (b) Step 21 (c) Step 33 (d) Step 39.

CARRIER CONCENTRATION

Zhao et al. determined carrier concentration in the structure via hall measurements[5]. We can observe that the carrier concentration is constant in the 300 K-600 K range which correspond to the Pnma phase. During the transition region (600 K-807 K), the carrier concentration rises exponentially. They also report anisotropic hall coefficients which leads to different carrier concentrations along cartesian axis. However, the determination of carrier concentrations with hall resistances assumes a single parabolic band model and a hall scattering factor of unity. Though this simple model fails to determine the exact carrier concentration because it should be isotropic along the different cartesian directions, it gives a good indication of the real value throughout the structure. Our calculations are carried out with a temperature dependent carrier concentration chosen to be the mean value of the carrier concentration along the three cartesian directions. We also extrapolate the curve for higher temperatures as measurement of hall coefficients stops at 823 K[5]. Several extrapolation schemes are performed and the one that is retained is the one that maximize the Seebeck coefficients for Cmcm phase in the range 824 K-1000 K. Lower or larger carrier concentrations result in a lower Seebeck coefficient. Our extrapolation shows that the exponential rise of the carrier concentration of the transition zone is stopped with the stabilization of the Cmcm phase at 807 K. Above that point, our results show that the carrier concentration continues to rise with a smaller pace. The creation of defects in the structure continues when the structure become Cmcm. The constant shape of the experimental conductivity and Seebeck coefficient for the Cmcm phase measured by Zhao et al. [5] confirms the rise of the carrier concentration with temperature. Indeed, as the temperature rises, the conductivity should decrease due to higher electron-phonon scattering. This decrease is compensated by the rise of carrier concentration. Similarly, the diminution of the band gap with temperature tends to decrease the Seebeck coefficient and is also compensated by increasing the amount of carriers in the structure. Fig. 8 shows the chemical potential plotted with the carrier concentration and the density of states of the 3 structures used to calculate the Seebeck coefficients. We can also split the analysis in 3. For the first structure, the experimental carrier concentration is approximately constant. The chemical potential rises slightly to counteract the temperature effects. During the phase transition (600 K - 800 K), the chemical potential is strongly lowered to populate the valence bands and to increase exponentially the carrier concentration. Finally, in the Cmcm region, the chemical potential stays constant as the rise of temperature is sufficient to ensure the rise of the carrier concentration.

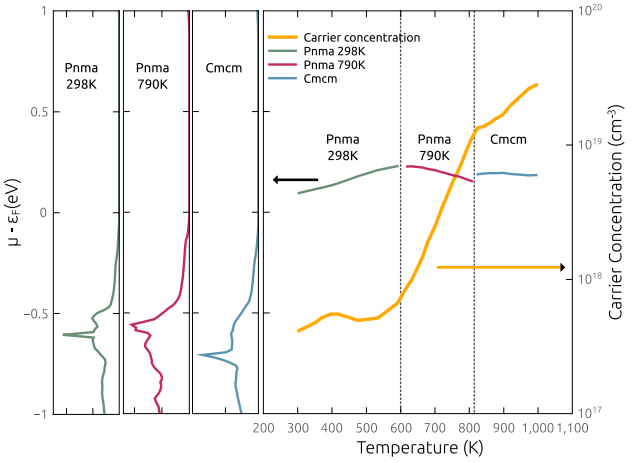

FIG. 8. Chemical potential of the 3 structures used to calculate Seebeck coefficients doped to fit the experimental carrier concentration.

DEFECT-THERMOCHEMISTRY CALCULATIONS

For the defect-thermochemistry calculations we consider the defects in their dilute limit [34–36]. The energy required to generate a defect, D, with charge q under given crystal growth condition is

$$E_{\rm d}({\rm D}^{(q)},\mu_e) = E_{\rm f}({\rm D}^{(q)}) + q\mu_e - \sum_\alpha n_\alpha \Delta\mu_\alpha. \quad (1)$$

Here, $E_{\rm f}({\rm D}^{(q)}) = E({\rm D}^{(q)}) - E_{\rm bulk} - \sum_\alpha n_\alpha E_\alpha$ is the defect formation energy expressed with respect to its natural state. $E({\rm D}^{(q)})$ is the total energy of the supercell containing the defect and $E_{\rm bulk}$ is the energy of the pristine host material. Furthermore, n_α is the number of atoms of element α that are transferred to the defected cell from the reservoir, E_α is the energy of the reference state and $\Delta\mu_\alpha$ is their corresponding chemical potentials. The chemical potential of the charge, $\mu_{\rm e}$, is expressed with respect to the valence band maximum (VBM) for the pristine cell. We considered charged defects with $q = [3, 2]$. In Fig. 2 (main paper), for each defect $D(q)$ at every μ_e value, we illustrate only the E_d for the most stable charged defect at a given μ_e. Consequently, the slope of E_d versus μ_e graph is the charge q for the defect.

Two different corrections to the defect energy are implemented, firstly due to difference in the alignment of the valence bands for the defected and pristine supercells and secondly the spurious electrostatic self-interactions due to the finite size of the supercells [34, 37]. The elemental chemical potentials ($\Delta\mu_{\rm Sn}$ and $\Delta\mu_{\rm Se}$) indicate the growth conditions. These are in principle variables, but must satisfy conditions that lead to a thermodynamically stable host and prevent the formation of competing phases. Note that the defect energies in Fig. 2 of the

main paper are illustrated at Se rich growth conditions which favours p-doping of SnSe by the virtue of stable Vac_{Sn} defects.

The concentration of defects, $c_{\mathrm{D}^{(q)}}$, is calculated using the procedure detailed in Refs. 34 and 35. Conservation of charge results in the following expressions,

$$n_e - n_h = \sum_{\mathrm{D}} q c_{\mathrm{D}^{(q)}}, \tag{2}$$

$$n_e = \int_{\varepsilon_{\mathrm{CBM}}}^{\infty} n(\varepsilon) f(\varepsilon;\mu_e)\, d\varepsilon \ , \ n_h = \int_{-\infty}^{\varepsilon_{\mathrm{VBM}}} n(\varepsilon)[1 - f(\varepsilon;\mu_e)]\, d\varepsilon$$

where n_e and n_h are the number of electrons and holes. $\varepsilon_{\mathrm{CBM}}$ and $\varepsilon_{\mathrm{VBM}}$ are the conduction band minimum (CBM) and VBM respectively, $f(\varepsilon;\mu_e)$ is the Fermi-Dirac distribution and $n(\varepsilon)$ is the DFT density of States. Here we approximate that the amount of defects in the host is small enough for the electronic structure of the defected super-cell to be equal to that of the host, i.e. the dilute limit. Boltzmann's distribution will result in the following expression for the temperature dependence of $c_{\mathrm{D}^{(q)}}$,

$$c_{\mathrm{D}^{(q)}} = c_0 \ \exp\left(\frac{-E_d(\mathrm{D}^{(q)})}{k_{\mathrm{B}}T}\right), \tag{3}$$

where c_0 is the number of the possible defect sites, E_d is the defect formation energy obtained from Eq. (1) and k_{B} is the Boltzmann's constant. The three simultaneous equations, Eq. (1), Eq. (2) and Eq. (3) are solved to obtain $c_{\mathrm{D}^{(q)}}$ at different temperature for each defect.

[1] X. Gonze, J.-M. Beuken, R. Caracas, F. Detraux, M. Fuchs, G.-M. Rignanese, L. Sindic, M. Verstraete, G. Zerah, F. Jollet, et al., Computational Materials Science **25**, 478 (2002).

[2] X. e. a. Gonze, Zeitschrift für Kristallographie **220**, 558 (2005).

[3] H. J. Monkhorst and J. D. Pack, Physical Review B **13**, 5188 (1976).

[4] G. Shi and E. Kioupakis, Journal of Applied Physics **117**, 065103 (2015).

[5] L.-D. Zhao, S.-H. Lo, Y. Zhang, H. Sun, G. Tan, C. Uher, C. Wolverton, V. P. Dravid, and M. G. Kanatzidis, Nature **508**, 373 (2014).

[6] Y. A. Timofeev, B. V. Vinogradov, and V. B. Begoulev, Physics of the Solid State **39**, 207 (1997).

[7] S. Sassi, C. Candolfi, J.-B. Vaney, V. Ohorodniichuk, P. Masschelein, A. Dauscher, and B. Lenoir, Applied Physics Letters **104**, 212105 (2014).

[8] T. Chattopadhyay, J. Pannetier, and H. V. Schnering, Journal of Physics and Chemistry of Solids **47**, 879 (1986).

[9] J. Carrete, N. Mingo, and S. Curtarolo, Applied Physics Letters **105**, 101907 (2014).

[10] R. Guo, X. Wang, Y. Kuang, and B. Huang, Physical Review B **92** (2015).

[11] X. Guan, P. Lu, L. Wu, L. Han, G. Liu, Y. Song, and S. Wang, Journal of Alloys and Compounds **643**, 116 (2015).

[12] P. Blaha, K. Schwarz, G. Madsen, D. Kvasnicka, and J. Luitz, An Augmented Plane WaVe Plus Local Orbitals Program for Calculating Crystal Properties. ISBN 3-9501031-1-2. Vienna University of Technology: Austria (2001).

[13] E. Engel and S. H. Vosko, Physical Review B **47**, 13164 (1993).

[14] M. Verstraete and Z. Zanolli, in *Computing Solids: Models, Ab-initio Methods and Supercomputing, Lecture Notes of the 45th Spring School 2014*, edited by S. Blügel, N. Helbig, V. Meden, and D. Wortmann, Forschungszentrum Jülich (Schriften des Forschungszentrums Jülich, Jülich, 2014), vol. 35 of *Schlüsseltechnologien Key Technologies*, pp. C2.1 – C2.29.

[15] A. H. Romero, E. K. U. Gross, M. J. Verstraete, and O. Hellman, Physical Review B **91** (2015).

[16] O. Hellman, P. Steneteg, I. A. Abrikosov, and S. I. Simak, Physical Review B **87**, 104111 (2013).

[17] O. Hellman and I. A. Abrikosov, Physical Review B **88**, 144301 (2013).

[18] P. E. Blöchl, Phys. Rev. B **50**, 17953 (1994).

[19] G. Kresse, Computational Materials Science **6**, 15 (1996).

[20] G. Kresse, Physical Review B **59**, 1758 (1999).

[21] G. Kresse and J. Furthmüller, Physical Review B **54**, 11169 (1996).

[22] G. Kresse and J. Hafner, Physical Review B **48**, 13115 (1993).

[23] J. P. Perdew, K. Burke, and M. Ernzerhof, Phys. Rev. Lett. **77**, 3865 (1996).

[24] S. Nosé, Molecular physics **52**, 255 (1984).

[25] W. G. Hoover, Physical Review A **31**, 1695 (1985).

[26] P. Steneteg, O. Hellman, O. Y. Vekilova, N. Shulumba, F. Tasndi, and I. A. Abrikosov, Physical Review B **87** (2013).

[27] R. Martoňák, A. Laio, and M. Parrinello, Physical review letters **90**, 075503 (2003).

[28] R. Martoňák, A. Laio, M. Bernasconi, C. Ceriani, P. Raiteri, F. Zipoli, and M. Parrinello, Zeitschrift für Kristallographie **220**, 489 (2005).

[29] R. Martoňák, The European Physical Journal B **79**, 241 (2011).

[30] S. Nosé, The Journal of chemical physics **81**, 511 (1984).

[31] S. Nose, Progress of Theoretical Physics pp. p1–117 (1991).

[32] D. Bylander and L. Kleinman, Physical Review B **46**, 13756 (1992).

[33] G. I. Csonka, J. P. Perdew, A. Ruzsinszky, P. H. Philipsen, S. Lebègue, J. Paier, O. A. Vydrov, and J. G. Ángyán, Physical Review B **79**, 155107 (2009).

[34] C. Bera, S. Jacob, I. Opahle, N. S. H. Gunda, R. Chmielowski, G. Dennler, and G. K. H. Madsen, Phys. Chem. Chem. Phys. **16**, 19894 (2014).

[35] S. Bhattacharya, N. S. H. Gunda, R. Stern, S. Jacobs, R. Chmielowski, G. Dennler, and G. K. H. Madsen, Phys. Chem. Chem. Phys. **17**, 9161 (2015).

[36] C. G. Van de Walle and J. Neugebauer, Journal of Applied Physics **95**, 3851 (2004).

[37] G. Makov and M. C. Payne, Physical Review B **51**, 4014 (1995).